

Received 14 January 2015

Accepted 6 June 2015

Edited by S. Svensson, Uppsala University, Sweden

Keywords: infrared synchrotron beamline; bending magnet; optical aberrations; optical path.

Optimized IR synchrotron beamline design

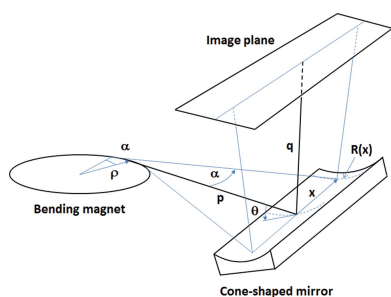
Thierry Moreno*

Experimental Division, Synchrotron SOLEIL, L'Orme des Merisiers, Saint-Aubain, BP 48, 91192 Gif sur Yvettes Cedex, France. *Correspondence e-mail: thierry.moreno@synchrotron-soleil.fr

Synchrotron infrared beamlines are powerful tools on which to perform spectroscopy on microscopic length scales but require working with large bending-magnet source apertures in order to provide intense photon beams to the experiments. Many infrared beamlines use a single toroidal-shaped mirror to focus the source emission which generates, for large apertures, beams with significant geometrical aberrations resulting from the shape of the source and the beamline optics. In this paper, an optical layout optimized for synchrotron infrared beamlines, that removes almost totally the geometrical aberrations of the source, is presented and analyzed. This layout is already operational on the IR beamline of the Brazilian synchrotron. An infrared beamline design based on a SOLEIL bending-magnet source is given as an example, which could be useful for future IR beamline improvements at this facility.

1. Introduction

The intense and transversally coherent radiation delivered by infrared (IR) synchrotron beamlines (Duncan & Williams, 1983; Schweizer *et al.*, 1985) makes the use of bending-magnet sources very attractive to perform micro-spectroscopy but requires highly collimated beams in order to match to the spectroscopic techniques, which mainly couple micro-scale mapping (Carr *et al.*, 1998; Dumas & Tobin, 2003) with Michelson interferometry (Jackson & Mantsch, 1995). Before collimation, the large source emission is first focused, usually using a single toroidal-shaped mirror, to create a secondary source at the exit of the front-end. This secondary source contains geometrical aberrations produced by the circular shape of the bending-magnet source that cannot be correctly removed by the toroidal mirror. These aberrations grow as the square of the horizontal beamline aperture and make it difficult to properly collimate the beam afterwards. This paper presents an optical design, consisting of two front-end mirrors, a cylindrical one focusing the horizontal emission of the IR source, and a cone-shaped one focusing the vertical emission. The geometrical aberrations produced by the source and the optics are analyzed using the optical path method (Noda *et al.*, 1974; Howells, 1992) and the best mirror configuration, removing source aberrations, is obtained. This method is then applied to the design of an IR beamline example based on a SOLEIL (Source Optimisée de Lumière à l'Energie Inter-médiaire du LURE) bending-magnet source (Level *et al.*, 2002). In this study, only the synchrotron radiation mode of IR emission is considered, but, since our optical layout removes the aberrations from all positions of the source trajectory, in particular at the entrance of the bending magnet, it also suits the edge radiation mode (Bosch *et al.*, 1996; Roy *et al.*, 2000). Although IR synchrotron radiation is almost fully transversely coherent, optical beam properties such as intensities, sizes and



divergences are here accurately described using a ray-tracing approach (Moreno & Idir, 2001).

2. Method

Synchrotron radiation emission occurs when relativistic electrons are accelerated radially by a magnetic field from a bending magnet, thus following a circular trajectory. The photon source size results from the convolution of three terms: the geometrical aberrations produced by the circular shape of the electron trajectory (synchrotron radiation mode), the electron beam size and the diffraction limit (Hecht & Zajac, 1987). When the geometrical aberrations are small in comparison with the two other terms, for example, for small beamline apertures or for very large wavelengths as in the far IR, the horizontal and vertical profiles of the photon source are Gaussian, whereas for large extraction apertures the geometrical aberrations prevail and the profiles maintain the aberrations of the source shape. In this case, the horizontal profile of the source emission resembles the one obtained from reflection through a cylindrical mirror and retains the aberrations resulting from the circular shape of the bending-magnet source. In the vertical direction, the profile is Lorentzian and is formed by the overlapping of all the vertical emissions produced at each point in the electron trajectory. In order to remove these aberrations resulting from the source geometry, two dedicated mirrors are used to focus separately the horizontal and vertical components of the source emission. This approach has been widely used and for a very long time in the soft and hard X-ray domains to design focusing optics (Kirkpatrick & Baez, 1948) and monochromators (Chen *et al.*, 1990).

2.1. Horizontal focusing mirror

Horizontally, the circular emission of the synchrotron radiation mode produces, for large horizontal beamline apertures, a beam profile containing coma aberrations (Hecht & Zajac, 1987) similar to the ones resulting from the reflection of a point source through a cylindrical mirror. So therefore, by using a cylindrical mirror in tangential reflection with a coma aberrated source, one can produce a point-like aberration-free image. The main parameters of this mirror such as its position inside the front-end, orientation and radius of curvature will be determined through the optical path method (Noda *et al.*, 1974; Howells, 1992). Fig. 1 shows the top view scheme of the cylindrical source (bending-magnet electron trajectory) and the cylindrical horizontal focusing mirror. The method minimizes the path distance between two rays, one emitted tangentially from the center of the circular source and reaching the center of the mirror and the image plane, and a second emitted with an angle α relatively to the central ray and reaching the same image position. The path difference is expressed as a Taylor expansion of the position w or the angle α (Fig. 1) with constant coefficients depending on the distances p and q between the center of the mirror and the center of the source and the image, respectively, the mirror grazing angle θ

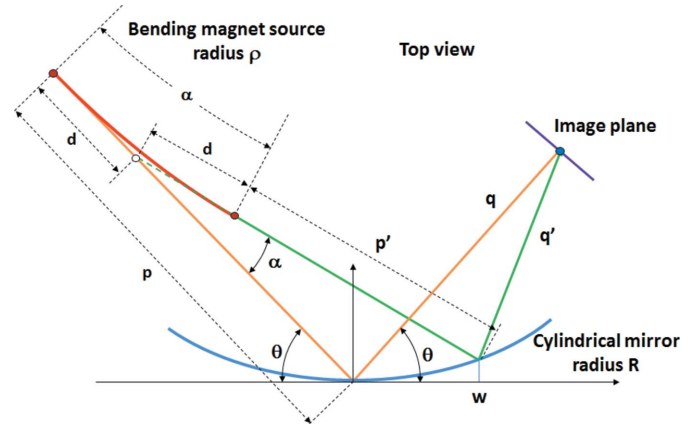


Figure 1

Horizontal source aberration scheme. A cylindrical mirror is used to remove the horizontal aberrations generated by the synchrotron radiation source (circular trajectory). The mirror position, orientation and radius of curvature are determined by minimizing the optical path difference $\Delta F_H = (p' + d + q') - (p - d + q)$.

and the radii of curvature of the mirror R and the source ρ (Fig. 1).

Since the optical path method is defined for a point light source, we consider here the source point resulting from the intersection of the two rays (Fig. 1) and the optical path difference $\Delta F_H = (p' + d + q') - (p - d + q)$ which depends on $d = \rho \tan(\alpha/2)$ (see Appendix A).

As the parameter d depends on α , the best choice is to express the path difference ΔF_H as a Taylor expansion of α , using the same notation as in Noda *et al.* (1974) and Howells (1992):

$$\Delta F_H = C_{10}\alpha + C_{20}\alpha^2 + C_{30}\alpha^3 + C_{40}\alpha^4 + \dots, \quad (1)$$

where C_{10} , C_{20} , C_{30} and C_{40} are the longitudinal tilt, longitudinal defocus, coma and the spherical aberration coefficients, respectively.

The coefficient C_{10} (tilt) is zero due to Fermat's principal (Hecht & Zajac, 1987) which imposes $C_{10} = \partial\Delta F_H/\partial\alpha|_{\alpha=0}$. The C_{20} (defocus) coefficient is

$$C_{20} = \frac{p^2}{2} \left[\frac{1}{p} + \frac{1}{q} - \frac{2}{R \sin(\theta)} \right], \quad (2)$$

where p , q , θ and R are the distances of the mirror to the central position of the circular source and the image plane, the grazing angle and the radius of curvature of the mirror, respectively (Fig. 1).

The full expressions of the C_{30} (coma) and C_{40} (spherical aberration) coefficients are quite complicated (see Appendix A) but can be simplified under certain conditions. When $C_{20} = 0$ (the lens equation), C_{30} simplifies to

$$C_{30} = \frac{p^3}{4 \tan(\theta)} \left(\frac{1}{p^2} - \frac{1}{q^2} \right) - \frac{\rho}{6}. \quad (3)$$

When $\theta \neq \pi/2$, C_{30} is zero for

$$q = p / \left[1 - \frac{2\rho \tan(\theta)}{3p} \right]^{1/2}. \quad (4)$$

Relation (4) generates two solutions, according to whether the curvatures of the mirror and the source trajectory are oriented in the same way ($\rho > 0$ and $q > p$) like in Fig. 1 or opposite ($\rho < 0$ and $q < p$). For $C_{20} = C_{30} = 0$, C_{40} simplifies to

$$C_{40} = \frac{p^4}{32 \tan^2(\theta)} \left(\frac{1}{p} + \frac{1}{q} \right) \left[\frac{p}{q} \left(\frac{3}{q} - \frac{1}{p} \right)^2 - \tan^2(\theta) \left(\frac{1}{p} - \frac{1}{q} \right)^2 \right]. \quad (5)$$

Combining equations (4) and (5), the grazing angle can be removed,

$$f(u) = \sqrt{u}(3u - 1) - \frac{3p}{2|\rho|}(1 - u^2)(1 - u) = 0, \quad (6)$$

with $u = p/q$.

The set of equations (2), (4) and (6) allows the determination of the best mirror configuration, removing the horizontal bending-magnet aberrations up to coefficient C_{40} included. As for (4), equation (6) gives two solutions depending of the source and mirror curvature orientation, $u < 1$ if the source and the mirror curvatures are oriented in the same way and $u > 1$ otherwise.

2.2. Vertical focusing mirror

In the vertical direction, the photon source size is made up of the overlapping of the radiation emitted all along the electronic trajectory. The vertical aberrations can be almost totally removed using a cone-shaped mirror. Fig. 2 shows a scheme of this mirror, oriented with its axis of curvature perpendicular to the source emission. Horizontally, the direction of the light emitted at any position from the source is centered tangentially to the electronic trajectory, so each source point of the trajectory is linked to the horizontal angle

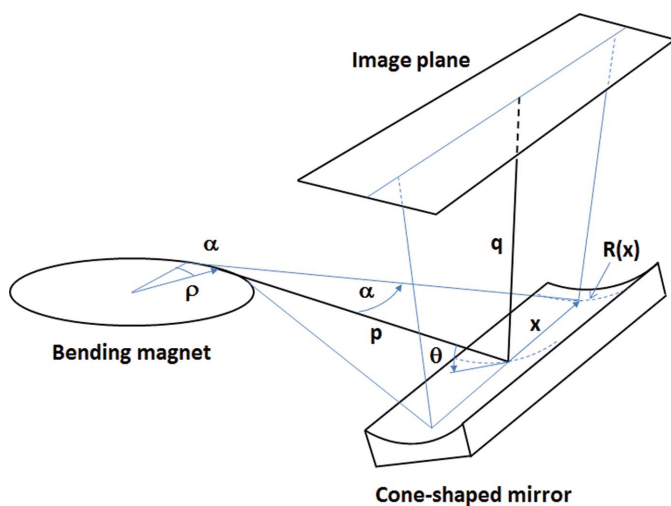


Figure 2
Cone-shaped mirror evaluation. The vertical aberrations generated by the synchrotron radiation source are removed with a cone-shaped mirror. The mirror cone section is determined by applying the lens equation to each ray emitted tangentially at the source.

of emission α . By applying the lens equation to each ray emitted tangentially to the source, the local radius of curvature at the position where the ray reaches the mirror can be determined and hence the shape of the mirror can be deduced. Relation (7) gives the Taylor expansion of the mirror radius obtained as a function of the position x along the mirror (Fig. 2),

$$R(x) = \frac{2pq}{\sin(\theta)(p+q)} \left\{ 1 - \frac{q\rho}{p^2(p+q)}x + \frac{1}{2p^2} \left[1 + \frac{p\rho^2(q-p)}{p^2(p+q)^2} \right] x^2 + \dots \right\}, \quad (7)$$

which corresponds to a cone-shaped mirror, where $R(x)$ is the local radius of curvature at the position x along the mirror, p and q are the source and image distances to the center of the mirror, ρ the bending-magnet radius and θ the mirror grazing angle. Since the mirror section is circular, the same method as the one presented in §2.1, but using a point light source ($\rho = 0$), can be applied to optimize the mirror position and orientation. Fig. 3 shows the side view scheme of the vertical mirror configuration. The optical path difference (Noda *et al.*, 1974; Howells, 1992) is given as a function of the angle φ between the two rays (Fig. 3):

$$\Delta F_V = (p' + q') - (p + q) = C_{10}\varphi + C_{20}\varphi^2 + C_{30}\varphi^3 + C_{40}\varphi^4 + \dots, \quad (8)$$

where C_{10} , C_{20} , C_{30} and C_{40} are the longitudinal tilt and defocus, coma and the spherical aberration coefficients of the optical path difference ΔF_V , respectively.

The aberration coefficients C_{20} , C_{30} and C_{40} are given by equations (2), (3) and (5) for a point light source ($\rho = 0$) and with the parameters p , q , R and θ of the vertical focusing mirror (Fig. 3).

For $C_{20} = 0$, the coefficient C_{30} vanishes either for $q = p$ or $\theta = \pi/2$ (Gauss illumination).

For $C_{20} = C_{30} = 0$, the coefficient C_{40} becomes

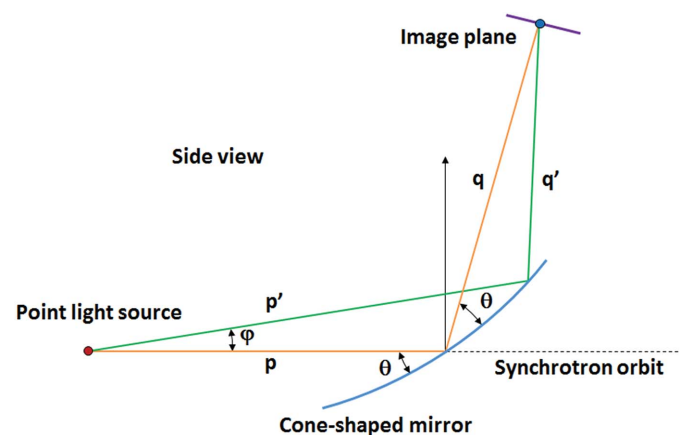


Figure 3
Vertical source aberration scheme. The mirror position, orientation and central radius of curvature are determined by minimizing the optical path difference $\Delta F_V = (p' + q') - (p + q)$.

$$C_{40} = \frac{p}{4 \tan^2(\theta)} \quad \text{for } q = p \quad \text{and} \quad (9)$$

$$C_{40} = -\frac{p^4}{32} \left(\frac{1}{p} + \frac{1}{q} \right) \left(\frac{1}{p^2} - \frac{1}{q^2} \right) \quad \text{for } \theta = \pi/2.$$

To summarize, the aberrations resulting from the vertical focusing mirror are removed up to the C_{30} coefficient, for either $p = q$ or $\theta = \pi/2$, and up to coefficient C_{40} if $p = q$ and $\theta = \pi/2$. In practice, $\theta \neq \pi/2$ and the best position for the vertical focusing mirror is half the distance from the source to the image plane ($p = q$).

For very large horizontal apertures, the intersection between the peripheral vertical beam emission and the mirror becomes non-circular and thus the vertical aberrations are less efficiently removed at the mirror borders.

2.3. Focused beam sizes

The beam size on the image plane σ_{tot} results from the convolution of the geometrical beamline aberrations σ_{geo} and the optical magnification M of both the electron beam size σ_e and the diffraction-limited size σ_{dlim} (when defined at the source location). Assuming Gaussian distributions, the horizontal and vertical beam size on the image plane is given by

$$\sigma_{\text{tot}} = \left[\sigma_{\text{geo}}^2 + (M\sigma_{\text{dlim}})^2 + (M\sigma_e)^2 \right]^{1/2}, \quad (10)$$

where $M = q/p$ is the magnification of the horizontal or the vertical focusing mirror. The horizontal and vertical electron beam sizes σ_{eX} and σ_{eZ} are determined by the accelerator design. The diffraction-limited size σ_{dlim} is related to the natural radial opening angle $2\theta_n$ of coherent emission of the bending magnet and depends on the working wavelength λ through the following equation (Bosch *et al.*, 1996) (for a fringe contrast of 50%):

$$\sigma_{\text{dlim}} = \frac{\lambda}{4\pi 2\theta_n} \quad \text{and} \quad \theta_n \text{ (rad)} = \left(\frac{3\lambda}{4\pi\rho} \right)^{1/3}. \quad (11)$$

This natural opening angle $2\theta_n$ also determines the coherent photon divergence of the bending-magnet emission.

The geometrical aberrations $\sigma_{\text{geo}X}$ and $\sigma_{\text{geo}Z}$ produced by the optical layout are obtained by integrating the ray aberrations $\Delta y = (q/p)\partial\Delta F/\partial\alpha$ over the full horizontal and vertical source divergences (Howells, 1992).

3. Application

The method described in §2 is now applied to the design of an IR beamline using a SOLEIL bending-magnet source. The beamline has an aperture of 80×40 mrad (H \times V) and a front-end distance of 12 m. The optical properties of the beamline are calculated by ray tracing at wavelengths of $\lambda = 1, 10$ and $100 \mu\text{m}$. Table 1 gives the electronic parameters of the source while Table 2 gives, from equation (11), the natural opening angle $2\theta_n$, the limit of diffraction size at the three wavelengths and the Gaussian source size resulting from the convolution of the electron source and the limit of diffraction.

Table 1
Source parameters.

Electron energy, intensity	$E_0 = 2.734 \text{ GeV}, I_0 = 0.5 \text{ A}$
Electron beam size	$\sigma_{eX} \times \sigma_{eZ} = 63.1 \times 32.4 \mu\text{m RMS (H} \times \text{V)}$
Bending magnet	$B = 1.72 \text{ T}, \rho = 5.28 \text{ m}$
Photon divergence	$\Delta'_X \times \Delta'_Z = 80 \times 40 \text{ mrad (H} \times \text{V)}$

Table 2
Natural opening angle, limit of diffraction and photon source size (H \times V).

λ (μm)	$2\theta_n$ (mrad) RMS	σ_{dlim} (μm) RMS	$\sigma_e \times \sigma_{\text{dlim}}$ (μm) RMS
1	7.1	11.7	64.2×34.5
10	15.4	51.7	81.6×61.0
100	33.1	229.0	237.5×231.3

In the horizontal direction, the position, orientation and radius of curvature of the cylindrical mirror is obtained by solving equations (2), (4) and (6). Fig. 4 shows, for the three wavelengths, the horizontal RMS beam size focused at $p + q = 12$ m (focal plane) as a function of the parameter $u = p/q$. As expected, two positions minimize the horizontal beam size according to the relative orientation of the mirror curvature with respect to the one of the source: $u < 1$ for opposite curvatures and $u > 1$ for curvatures with the same sign.

From relation (6), the two configurations minimizing the geometrical aberrations are $u = 0.521$ and $u = 2.022$. By taking into account the electron beam size and the limit of diffraction, Fig. 4 shows that both minima are shifted to higher values of u due to the convolution of equation (10). Because of the horizontal magnification of the optical system, the minimum horizontal beam size is obtained in the region $u > 1$. This is the solution we choose for the optical design of our example. With a horizontal beamline aperture of 80 mrad, the best configuration allowing the beam to pass through the front end (see Fig. 5) is to choose $u = 1.9$, which defines the parameters of the horizontal correcting mirror: $p = 7862$ mm, $q = 4138$ mm, $\theta = 80.27^\circ$ and $R = 5501.3$ mm. In this configuration, the curva-

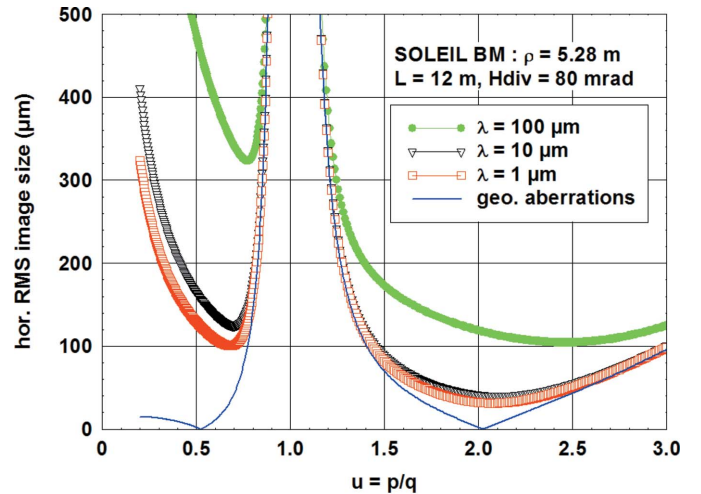


Figure 4
Horizontal beam size on the focal plane (12 m from the source) as a function of $u = p/q$.

tures of the source and the mirror are opposed. The vertical focusing mirror is placed at the same distance to the source and to the image plane ($p = q = 6$ m) in order to remove the vertical C_{20} and C_{30} aberration coefficients. There is no gain in resolution by increasing, according to equation (9), the mirror grazing angle to reduce the C_{40} aberration, because the limit of diffraction at the working wavelengths is far larger than the spherical aberration of the vertical focusing mirror at the defined position. The best configuration is to set its grazing angle at 45° to facilitate the alignment of the front-end optics. With a grazing angle of $\theta = 45^\circ$ (upward reflection), the best cone-shaped profile $R(x) = R_0(1 + ax)$ is obtained from equation (7) for $R_0 = 8485.3$ mm and $a = -7.333 \times 10^{-5} \text{ mm}^{-1}$ where x is the coordinate along the axis of curvature of the mirror.

Fig. 5 and Table 3 give the main parameters of our IR beamline example, where mirror positions are given as optical path distances from the source. The beamline consists of two optical stages: the focusing stage inside the front end including the first M1 mirror (using a horizontal 4 mm slot to remove the hard X-ray components of the bending-magnet emission), the cone-shaped mirror M4 and the cylindrical mirror M5, both focusing the 80×40 mrad (H \times V) bending-magnet emission on a focal plane located at 12 m from the source; and the collimating stage, made up of two parabolic shape mirrors (M7

Table 3
Parameters of the SOLEIL IR beamline example.

Element	Optical path distances	Geometry	Length \times width at $\lambda = 100 \mu\text{m}$
Diaphragm	1.0 m	80 mm \times 40 mm (H \times V)	
M1 mirror	1.3 m	Plane, slot of 4 mm $\theta = 45^\circ$, upward	77 mm \times 103 mm
M2 mirror	2.3 m	Plane $\theta = 45^\circ$, downward	115 mm \times 159 mm
M3 mirror	5.7 m	Plane $\theta = 45^\circ$, downward	315 mm \times 450 mm
M4 mirror	6.0 m	Cone shaped, vertical focus $\theta = 45^\circ$, upward	331 mm \times 474 mm
M5 mirror	7.862 m	Cylinder, horizontal focus $\theta = 80.27^\circ$, sideward	626 mm \times 162 mm
M6 mirror	9.862 m	Plane $\theta = 80.27^\circ$, sideward	324 mm \times 84 mm
CVD window	11.95 m		\varnothing 20 mm
Focal plane	12.0 m		
M7 mirror	12.5 m	Parabola, vertically collimating $\theta = 45^\circ$, downward	106 mm \times 20 mm
M8 mirror	13.3 m	Plane $\theta = 45^\circ$, upward	72 mm \times 75 mm
M9 mirror	14 m	Parabola, horizontally collimating $\theta = 45^\circ$, sideward left	75 mm \times 110 mm

and M9) collimating the beam to the experimental setup. These two mirrors are positioned in order to produce a collimated beam with a square shape at $\lambda = 100 \mu\text{m}$ (far IR).

Fig. 6 shows the ray-tracing simulation of the beam image at 12 m (focal plane) and 16 m (2 m after the last M9 mirror) from the source, respectively. Table 4 gives the corresponding beam sizes values and Table 5 the divergences and intensities delivered by the IR beamline. Since ray tracing propagates the light incoherently, contrary to beam propagation codes like *SRW* (Chubar & Elleaume, 1998), it does not take into account IR diffractions resulting from mirror slots (M1) nor

mirrors borders. Nevertheless, it is an accurate method to evaluate both geometrical aberrations resulting from bending-magnet sources and optical surfaces and beam properties such as intensities (outside diffractive areas), sizes and divergences. Thus, ray tracing is an efficient way to design and optimize IR synchrotron beamlines.

4. Conclusions

In this paper, an optical layout adapted to IR synchrotron beamlines is presented and analyzed. This layout consists of two shape-optimized mirrors, focusing separately the vertical and the horizontal emission of the bending-magnet source. It has been optimized using an analytical formulation based on the optical path method (Noda *et al.*, 1974; Howells, 1992). It removes almost totally the optical aberrations generated by the beamline components and

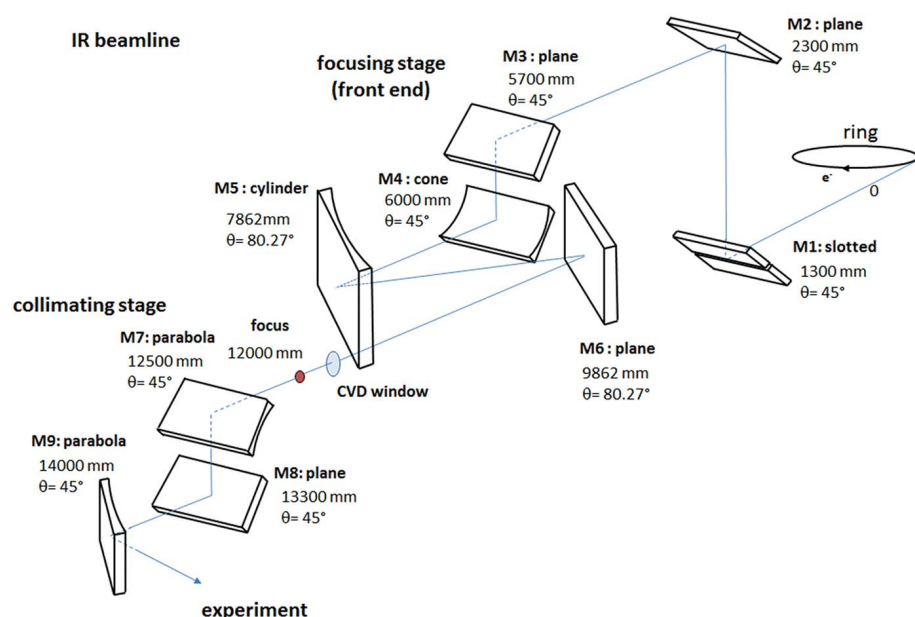


Figure 5
Optical scheme of the SOLEIL IR beamline example. The positions of the mirrors are given according to optical path distances from the source.

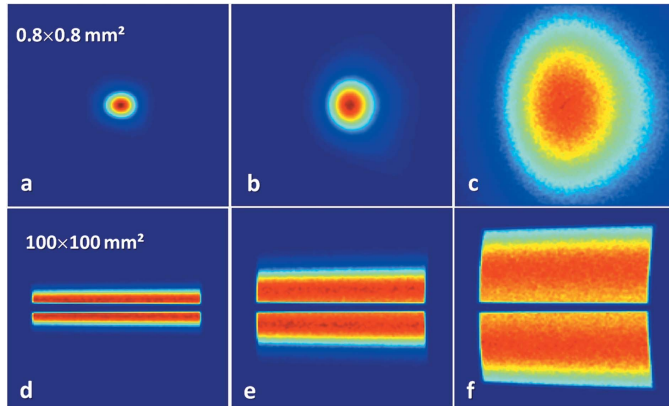


Figure 6
Image of the beam calculated by ray tracing: (a), (b), (c) Beam image at $\lambda = 1, 10, 100 \mu\text{m}$ on a screen of $0.8 \text{ mm} \times 0.8 \text{ mm}$ at the focal plane (12 m from the source). (d), (e), (f) Beam image at $\lambda = 1, 10, 100 \mu\text{m}$ on a screen of $100 \text{ mm} \times 100 \text{ mm}$ located 2 m after M9 (16 m from the source).

provides high collimated beams for large horizontal beamline apertures. This optical layout is already operational on the LNLS (Laboratórios Nacionais de Luz Síncrotron) IR beamline (Moreno *et al.*, 2013), the main conclusions being that it is efficient, easy to align and inexpensive to produce. A similar optical layout has been proposed and accepted for the future IR beamline at the ALS (Advanced Light Source). An IR beamline design using a SOLEIL bending-magnet source and working at $\lambda = 1, 10$ and $100 \mu\text{m}$ is given as an example, which could be useful for future IR beamline improvements at SOLEIL.

APPENDIX A Minimization of the horizontal bending-magnet aberrations

The optical path method is applied to the difference ΔF between the two paths $(p' + d) + q'$ and $(p - d) + q$ as defined in the scheme of Fig. 1, corresponding to the tangential reflection through a cylindrical mirror of a circular light source. ΔF is usually expressed as a Taylor expansion of the position w along the mirror (see Fig. 1):

$$\Delta F = A_{10}w + A_{20}w^2 + A_{30}w^3 + A_{40}w^4 + \dots, \quad (12)$$

where A_{10}, A_{20}, A_{30} and A_{40} are the longitudinal tilt, defocus, coma and the spherical aberration coefficients of ΔF , respectively, themselves a function of the angle α between the two rays through the parameter $d = \rho \tan(\alpha/2)$. For a cylindrical mirror, these aberration coefficients are well known and defined as (Howells, 1992):

$$A_{10} = \left. \frac{\partial \Delta F}{\partial w} \right|_{w=0} \quad (13)$$

is null due to Fermat's principal;

$$A_{20} = \frac{T_1 + T_2}{2}, \quad (14)$$

Table 4
Beam sizes (H \times V) at the focal plane and 2 m after the last mirror.

λ (μm)	Size (μm FWHM) At the focal plane	Size (mm at 99%) 2 m after M9
1	90×79	75×22
10	136×160	75×47
100	440×580	75×78

Table 5
Beam divergences (H \times V) and intensities after the last mirror.

λ (μm)	Divergence (μrad FWHM)	Flux (photons s^{-1} $0.1\% \text{ BW}^{-1}$)
1	180×40	2.3×10^{14}
10	275×80	1.3×10^{14}
100	874×290	5.7×10^{13}

$$A_{30} = \frac{\cos(\theta)}{2} \left(\frac{T_1}{p-d} - \frac{T_2}{q} \right), \quad (15)$$

$$A_{40} = -\frac{\sin(\theta)}{4R^3} + \frac{1}{8R^2} \left(\frac{1}{p-d} + \frac{1}{q} \right) + \frac{\cos^2(\theta)}{2} \left[\frac{T_1}{(p-d)^2} + \frac{T_2}{q^2} \right] - \frac{1}{8} \left(\frac{T_1^2}{p-d} + \frac{T_2^2}{q} \right), \quad (16)$$

with

$$T_1 = \frac{\sin^2(\theta)}{p-d} - \frac{\sin(\theta)}{R}, \quad T_2 = \frac{\sin^2(\theta)}{q} - \frac{\sin(\theta)}{R}.$$

The tricky development of $d = (\rho/2)\alpha - (\rho/24)\alpha^3 + \dots$ inside A_{20}, A_{30} and A_{40} and α inside w allows us to develop ΔF as a function of constant coefficients of α , as defined by relation (1), where C_{10}, C_{20}, C_{30} and C_{40} are now independent of α and w .

Acknowledgements

The author thanks Paul Dumas for the very active and fruitful collaboration in the development of IR beamlines and Yves Petroff, Raul Freitas and Harry Westfalh Jr for their confidence in our optical layout and the very nice results obtained on their LNLS IR beamline. The author also thanks Michael Martin and Hans A. Bechtel for having accepted our design for the future ALS IR beamline.

References

- Bosch, R. A., May, T. E., Reininger, R. & Green, M. A. (1996). *Rev. Sci. Instrum.* **67**, 3346.
- Carr, G. L., Dumas, P., Hirschmug, C. J. & Williams, G. P. (1998). *Nouv. Cim. D*, **20**, 375–395.
- Chen, C. T., Sette, F. & Smith, N. V. (1990). *Appl. Opt.* **29**, 4535–4536.
- Chubar, O. & Elleaume, P. (1998). *Proceedings of the Sixth European Particle Accelerator Conference (EPAC'98)*, pp. 1177–1179.
- Dumas, P. & Tobin, M. J. (2003). *Spectrosc. Eur.* **15**, 17–23.
- Duncan, W. D. & Williams, G. P. (1983). *Appl. Opt.* **22**, 2914–2923.
- Hecht, E. & Zajac, A. (1987). *Optics*, 2nd ed. Reading: Addison Wesley.
- Howells, M. R. (1992). *Proceedings of the NATO Advanced Study Institute on New Directions in Research with Third-Generation Soft*

- X-ray Synchrotron Radiation Sources*, Maratea, Italy, 28 June–10 July 1992, NATO ASI Series E: Applied Sciences, Vol. 254, p. 359. Dordrecht: Kluwer.
- Jackson, M. & Mantsch, H. H. (1995). *Crit. Rev. Biochem. Mol. Biol.* **30**, 95–120.
- Kirkpatrick, P. & Baez, A. V. (1948). *J. Opt. Soc. Am.* **38**, 766–774.
- Level, M.-P., Brunelle, P., Chaput, R., Filhol, J.-M., Herbeaux, C., Loulergue, A., Marcouille, O., Marlats, J.-L., Nadji, A. & Tordeux, M.-A. (2002). *Proceedings of the Eighth European Particle Accelerator Conference (EPAC'02)*, pp. 212–214.
- Moreno, T. & Idir, M. (2001). *J. Phys. IV Fr.* **11**, 527–531.
- Moreno, T., Westfahl, H., Freitas, R. de O., Petroff, Y. & Dumas, P. (2013). *J. Phys. Conf. Ser.* **425**, 142003.
- Noda, H., Namioka, T. & Seya, M. (1974). *J. Opt. Soc. Am.* **64**, 1037–1042.
- Roy, P., Guidi Cestelli, M., Nucara, A., Marcouille, O., Calvani, P., Giura, P., Paolone, A., Mathis, Y. L. & Gerschel, A. (2000). *Phys. Rev. Lett.* **84**, 483–486.
- Schweizer, E., Nagel, J., Braun, W., Lippert, E. & Bradshaw, A. M. (1985). *Nucl. Instrum. Methods Phys. Res. A*, **239**, 630–634.